

A machine-learning interatomic potential to study dry/wet oxidation process of silicon

Cite as: J. Appl. Phys. 136, 095302 (2024); doi: 10.1063/5.0219764

Submitted: 20 May 2024 · Accepted: 17 August 2024 ·

Published Online: 3 September 2024



View Online



Export Citation



CrossMark

Huyang Li,¹ Yuhang Jing,^{1,a)} Zhongli Liu,² Lingzhi Cong,¹ Junqing Zhao,¹ Yi Sun,¹ Weiwei Li,³ Jihong Yan,⁴ Jianqun Yang,² and Xingji Li^{2,a)}

AFFILIATIONS

¹Department of Astronautical Science and Mechanics, Harbin Institute of Technology, Harbin, Heilongjiang 150001, China

²Technology Innovation Center of Materials and Devices at Extreme Environment, Harbin Institute of Technology, Harbin, Heilongjiang 150001, China

³School of Physics, Harbin Institute of Technology, Harbin, Heilongjiang 150001, China

⁴Laboratory for Space Environment and Physical Sciences, Harbin Institute of Technology, Harbin, Heilongjiang 150001, China

^{a)}Authors to whom correspondence should be addressed: jingyh@hit.edu.cn and lxj0218@hit.edu.cn

ABSTRACT

We developed an accurate and efficient machine learning potential with DFT accuracy and applied it to the silicon dry/wet oxidation process to investigate the underlying physics of thermal oxidation of silicon (001) surfaces. The accuracy of the potential was verified by comparing the melting point and structural properties of silicon, the structural properties of a-SiO₂, and the adsorption properties on the silicon surface with experiment and DFT data. In subsequent thermal oxidation simulations, we successfully reproduced the accelerated growth phenomenon of the wet oxidation in the experiment, discussed the oxide growth process in detail, and elucidated that the accelerated growth is due to hydrogen in the system that both enhances the adsorption of oxygen on the silicon surface and promotes the migration of oxygen atoms. Finally, we annealed the oxidized structure, counted the defect information in the structure before and after annealing, and analyzed the defect evolution behavior during the annealing process.

© 2024 Author(s). All article content, except where otherwise noted, is licensed under a Creative Commons Attribution (CC BY) license (<https://creativecommons.org/licenses/by/4.0/>). <https://doi.org/10.1063/5.0219764>

07 September 2024 09:05:31

I. INTRODUCTION

Since the advent of metal oxide semiconductor field effect transistors (MOSFETs) in the 1960s, silicon-based MOSFETs have occupied an important place in modern electronic devices. In silicon-based MOSFETs, a layer of silicon dioxide grown on a silicon substrate by the oxidation process is an excellent choice for a MOSFET gate dielectric because of its extremely high dielectric constant.¹ According to the model developed by Deal and Grove,² the oxidation process proceeds in the following manner: in the initial stage, the oxidants (H₂O and O₂) come into direct contact with Si and react to form SiO₂, and when an oxide layer exists on the surface, the oxidants will diffuse through the already existing oxide layer to the Si/SiO₂ interface, where it reacts with Si to form SiO₂. The Deal-Grove model accurately describes the growth process of SiO₂ in the range of 300–20 000 Å thickness on the silicon surface. However, for recent devices such as FinFETs, which

contain an oxide layer of a few nanometer thicknesses, the conventional Deal-Grove model will not be applicable.³ In addition, the presence of suboxide Si ions and Si defects in the interface region will affect the properties of the device, and these effects increase as the size of the electronic device decreases.^{4–6} Therefore, a detailed understanding of the silicon oxidation process and interface structure on a microscopic scale is important to enhance the properties of the current sub-nano scale device.

Advanced techniques such as x-ray diffraction spectroscopy, x-ray photoelectron spectroscopy, and optical spectroscopy are often used by experimentalists to study oxidation.⁷ Based on these techniques, although it is possible to identify information about the structure and defects of the oxides produced by oxidation, these techniques are not able to understand the oxidation process on the silicon surface on a microscopic scale because they lack the means to observe the motion of the atoms. To address this problem, the

use of atomic-scale simulations to provide a microscopic view is necessary. Moreover, the mechanisms by which different process conditions such as oxidation temperature, dry oxidation, and wet oxidation affect the nature of the oxide layer need to be explored with the help of simulation. The Density Functional Theory (DFT) method provides relatively accurate Born–Oppenheimer potential energy surfaces that can be used to obtain the reaction barrier for oxidation, the oxygen molecules migration path on the silicon surface during oxidation, and the stable atomic configurations after oxidation.^{8–10} However, due to the limitations of this approach on spatial and time scales, it is difficult to detail the simulation that is comparable with experiments. Compared to the DFT approach, classical molecular dynamics (MD) simulations are more computationally efficient and can handle larger spatial and time scales. Some researchers have developed a charge-transfer interatomic potential based on the hybrid-Tersoff potential to grow amorphous SiO₂ (a-SiO₂) layers by incorporating oxygen molecules into the Si network at the interface, which recreates the thermo-oxidative growth process of silicon.¹¹ Furthermore, reactive force fields (ReaxFF) have also been widely used in atomic-scale simulations of silicon oxidation.¹² Many academics developed reactive force fields describing the Si/O/H interactions,^{13,14} which correctly characterize the radial distribution functions, densities, and bond lengths and angles of silicon and a-SiO₂, as well as the underlying mechanisms of oxygen diffusion in the silicon network, but could not reflect the experimental phenomenon that the rate of oxidation by wet is faster than that of dry oxidation. The reactive force field developed by Noaki *et al.* showed faster oxidation of silicon by the mixture of hydrogen and oxygen than by pure oxygen, but it could not roundly simulate the real wet oxidation process because it could not characterize the decomposition of the water molecules on the silicon surface.¹⁵ In addition, these empirical potentials usually overestimate the melting point of silicon. Temperature is an important parameter of the silicon oxidation process, and overestimating the melting point can lead to a misestimation of the silicon surface state at different temperatures, which can lead to a decrease in simulation accuracy. The reason for these problems is the lack of empirical potential accuracy; therefore, it is necessary to develop a potential with accuracy and efficiency to simulate silicon oxidation.

Recently, with the advancement of computer arithmetic power and machine learning (ML) algorithms, machine learning (ML) techniques have been applied to potential development in order to obtain machine learning potentials to improve the reliability of MD calculations.^{16–19} The ML potentials take DFT results as a dataset to train the mapping between the local atomic environments and the atomic energy contributions based on a purely mathematical structure such as a neural network or Gaussian process.²⁰ By this means, the ML potential successfully builds a bridge between DFT and MD, and it achieves a potential energy surface with DFT accuracy while maintaining the efficiency of MD simulations. Moreover, the ML potential is highly versatile in terms of application objects and application environments and can be applied to different types of materials such as Si,^{21,22} Cu,^{23,24} H₂O,¹⁶ BaZrO₃,^{25,26} Ga₂O₃,²⁷ etc., and also well describes the interactions between atoms in complex environments such as high temperature,²⁸ high pressure,²⁹ and irradiation.^{30,31}

In this paper, we constructed a database using DFT calculations and developed an ML potential with DFT accuracy to describe the thermal oxidation process of silicon. Based on the obtained model, we first calculated the melting point and structural properties of silicon, the structural properties of a-SiO₂, and the adsorption properties on the silicon surface to verify the accuracy of the ML potential. Then, the results of our MD simulation on the thermal oxidation are shown, discussing the growth process of the oxides in detail, elucidating the accelerating mechanism of wet oxidation. Finally, we annealed the oxidized structure, counting the defect information in the structure before and after annealing and analyzing the defect evolution behavior during the annealing process.

II. MACHINE LEARNING POTENTIAL

A. Database

We built a dataset related to oxidation conditions to train ML models that can describe the dry/wet oxidation process of silicon. The dataset contains three sections on static properties of silicon and silica, point defects in silicon and silica, and dry/wet oxidation processes of silicon, see Table I for specific details. The dataset contains a total of 175 460 conformations, all configurations were obtained using *ab initio* MD (AIMD) simulations. The type and number of configurations are based on physical intuition and past practice.

DFT calculations were performed with the Vienna *Ab initio* Simulation Package (VASP),^{32–34} using an enhanced projection wave method³⁴ and PBE generalization function.³⁵ The truncation energy of the plane wave basis was set to 500 eV. The NVT ensemble was selected for the AIMD simulation, and a Nosé–Hoover thermostat was used for temperature control. The time step for all simulations was set to 0.5 fs. A $2 \times 2 \times 2$ Monkhorst–Pack k-points mesh was used in static properties and defects related to properties AIMD simulations, and a $2 \times 2 \times 1$ Monkhorst–Pack k-points mesh was used in silicon oxidation process AIMD simulations. DFT calculated the potential energy for every configuration and the force per atom in the dataset and used it as a dataset for machine learning training.

B. Model training

Utilizing the DeePM^{16,36,37} artificial neural network architecture, the ML potential is trained based on the obtained dataset. For training, 80% of the dataset is designated as the training set, while the remaining portion serves as the test set. Local atomic environments consider atoms within a truncation radius of 6 Å as an ML potential. The descriptor of the local atomic environment is a hybrid descriptor, comprised of se_e2_a and se_e2_r. Both are the two-body embedding smooth edition of the DP descriptor, the former constructs the descriptor using full relative coordinates, while the latter utilizes radial-only information to build the descriptor. The local atomic environment is mapped to the energy contribution of the atoms to the system by deep neural network containing three hidden layers, each containing 240 neurons, and hyperbolic tangent (tanh) function is chosen as the activation function embedded in the network. The start learning rate for training

TABLE I. Summary of databases used for silicon oxidation model training. The first column shows the corresponding properties of the configurations. The second column shows the type of configurations. The third column shows the number of atoms of the configurations. The fourth column shows the number of configurations. The last column shows the number of atomic environments, which is equal to the number of atoms times the number of configurations.

Corresponding properties	Structure type	No. atoms	No. configurations	No. atomic environments
Static properties	Diamond Si	64	70 000	4 480 000
	Amorphous SiO ₂	648	4 000	2 592 000
	low quartz SiO ₂	72	6 000	432 000
	Diamond Si surface (100)	144	9 000	1 296 000
Defects related properties	Diamond Si with vacancy	215	8 000	1 720 000
	Diamond Si with dumbbell interstitial	217	8 000	1 302 000
	Amorphous SiO ₂ with oxygen deficiency center	647	4 000	2 588 000
	Amorphous SiO ₂ with peroxy linkage	649	4 000	2 596 000
Silicon oxidation process	Dry oxidation	144	5 000	720 000
		160	7 500	1 200 000
		448	8 660	3 879 680
		131	15 000	1 965 000
	Wet oxidation	136	6 000	816 000
		147	4 000	588 000
		159	2 000	318 000
		162	4 000	648 000
		457	10 300	4 707 100

is set to 5×10^{-3} and the stop learning rate is 5×10^{-8} , and the learning rate will decay exponentially during the training process. The batch size for training is 4, and a total of 2×10^6 batches were trained for 57 epochs. Finally, observe the training error and testing error to evaluate whether overfitting occurs. Ideally, the training error and testing error should be roughly the same, while in a model with overfitting, there will be significantly larger testing errors. When overfitting occurs, it is advisable to either decrease the number of layers or neurons per layer, or alternatively, augment the size of the training dataset followed by a retraining process.

Figure 1 illustrates the results of the comparison of the energy and force of the ML potential with the reference DFT. During this training, the root mean square error (RMSE) of the training set is 4.42 meV/atom for energy and 165.82 meV/Å for force, the RMSE of the test set is 4.40 meV/atom and 168.68 meV/Å for energy and force; the mean absolute error (MAE) of the training set is 3.23 meV/atom for energy and 113.67 meV/Å for force, the MAE of the test set is 3.22 meV/atom for energy and 114.34 meV/Å for force. All of the RMSE values and the MAE values are within the range of reasonable values for the ML model.³⁸

III. RESULT AND DISCUSSION

A. Calculating melting point of crystalline silicon by two-phase method

Based on the ML potential, ReaxFF_{Larsson},¹³ and ReaxFF_{SiOH(2023)},¹⁵ we precisely calculated the melting point of crystalline silicon by a two-phase method.³⁹ The simulation box has dimensions of $43.4566 \times 43.4566 \times 54.307$ Å³ with periodic boundary conditions in all directions and contains a total of 5200 silicon atoms. Freezing of atoms in the lower half of the z-direction and melting of atoms in the upper half under the NVT ensemble are observed.

Melting was performed at 4000 K during 10 ps and followed by a ramp-down to the target temperature at a rate of 10 K/ps. The simulation box at this moment consists of both solid and liquid silicon [shown in Fig. 2(a)], each part containing 2560 atoms. Next, the NPT ensemble was chosen to relax the structure at the target temperature to observe which of the two phases would grow during relaxation. When the solid phase grows [shown in Fig. 2(b)], it indicates that the target temperature is below the melting point of silicon, and when the liquid phase grows [shown in Fig. 2(c)], it is above the melting point of silicon. The simulation stop is signaled by the fact that the simulation box is eventually filled by a phase. This process was repeated at different temperatures by using an ML potential, ReaxFF_{Larsson} and ReaxFF_{SiOH(2023)}, until obtaining the melting point of crystalline Si.

Snapshots of the two-phase MD simulation are shown in Fig. 2. Under the ML potential simulation, the simulation box is completely occupied by the solid phase at 1370 K, whereas the liquid phase filled the simulation box at 1375 K. The melting point of crystalline silicon is between 1370 and 1375 K. This value is close to the value of the melting point calculated by Hong using first principles.⁴⁰ ReaxFF_{Larsson} reached the melting temperature between 2365 and 2370 K, and ReaxFF_{SiOH(2023)} reached the melting temperature between 3440 and 3445 K. The melting point obtained experimentally was 1683 K, compared to the experimental value, an error of -18.5% for ML, an error of 40.6% for ReaxFF_{Larsson}, and an error of 104.5% for ReaxFF_{SiOH(2023)}.

Meanwhile, we also calculated several structural properties of Si using the ML potential and compared them with ReaxFF_{Larsson}, ReaxFF_{SiOH(2023)}, DFT results, and experiments. The structural properties here include the lattice constant a , the cohesive energy E_{Coh} , density, and Si–Si bond length d_{Si-Si} . The detailed results are shown in Table II. As evident from Table II, the computed

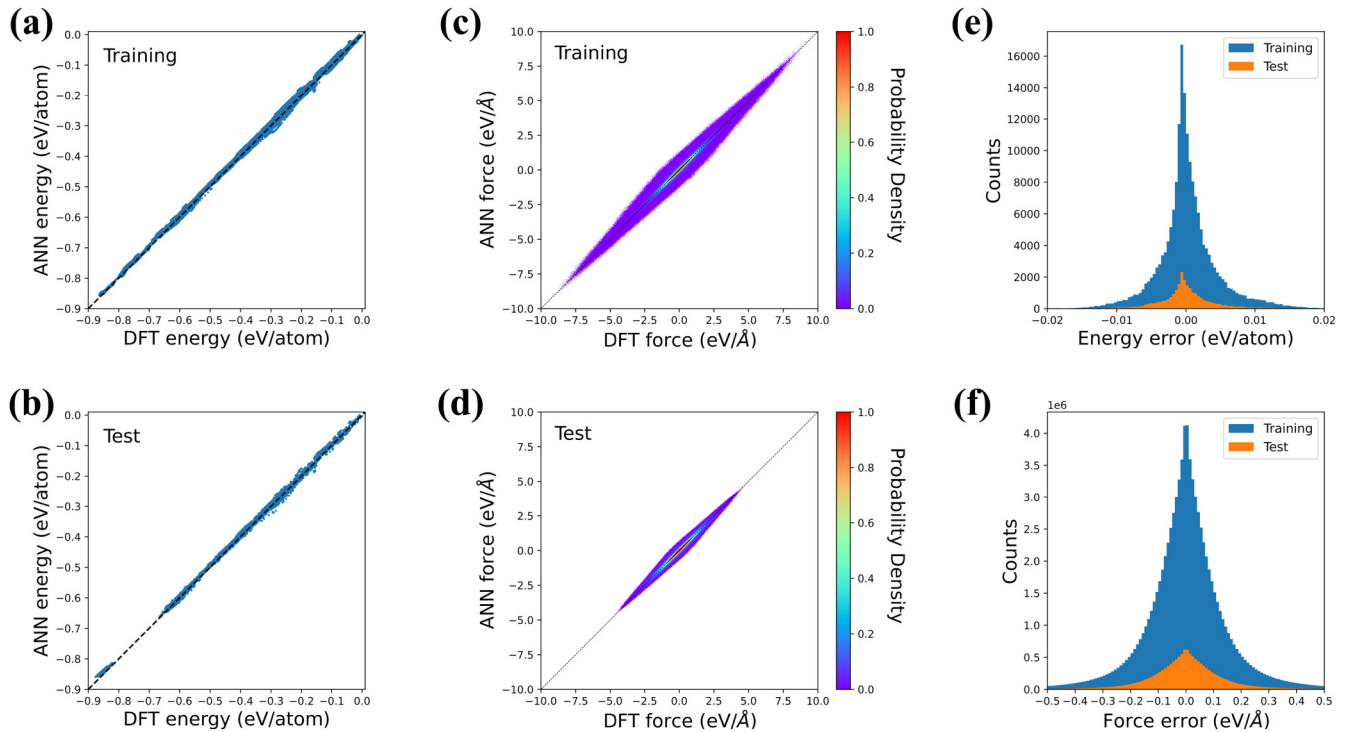


FIG. 1. Comparisons of the ML results with respect to the references DFT data. (a) and (b) show the comparisons of energies per atom for the training and test set, respectively. (c) and (d) exhibit force comparisons for the training and test set. 2D histogram plots are used to show the density distribution of errors. (e) and (f) display the error distributions for energies and forces for training and test set.

07 September 2024 09:05:31

structural properties based on our trained ML potential are very close to the DFT reference result and experimental values. For both versions of ReaxFF, the lattice constant is underestimated, and the density is overestimated. The results for the cohesive energy by ReaxFF_{SiOH(2023)} are also in error from the reference values. It is easy to see that the calculated structural properties by Reaxff are also not as good as the ML models.

B. The properties of amorphous SiO₂

In addition to the melting point and structural properties of Si, the properties of a-SiO₂, which is a product of the thermal oxidation process, are also important to focus on. We studied the properties of a-SiO₂ by the MD simulation based on ML potential, ReaxFF_{Larsson} and ReaxFF_{SiOH(2023)} and compared them with DFT results and experiments. The properties of a-SiO₂ considered include density; the average bond distances of Si–O, Si–Si, and O–O; the RDF first peaks of Si–O, Si–Si, and O–O; and the peaks of Si–O–Si and O–Si–O angle. The a-SiO₂ structure used in MD simulations and DFT simulations was derived from materials science simulation software Materials Studio, developed by American Accelrys. The structure is cubic with a dimension of 21.3949 Å with periodic boundary conditions and contains 432 O atoms and 216 Si atoms. The results of the properties of a-SiO₂ calculations are shown in Table III.

From Table III, using the ML potential obtained from our training, our calculated properties of a-SiO₂ are in good agreement with the DFT results and also consistent with the experiments. Most of the simulation results for both versions of ReaxFF are in conformity with DFT and experimental values, except for the Si–O–Si angle. ReaxFF_{Larsson} and ReaxFF_{SiOH(2023)} predict that most of the Si–O–Si angles are centered around 144.9° where there is a slight difference of 6.1° from the experimental values. Consequently, the ML potential can better characterize the properties of a-SiO₂ than other Reaxff.

C. Adsorption energy

Adsorption of the oxidizer on the substrate surface is a crucial aspect in the oxidation process. Therefore, the ML potential must accurately reproduce the adsorption-related properties like the average adsorption energies. The average adsorption energies have been calculated according to the following equation:⁴⁸

$$-E_{\text{ads}} = \frac{E_{(\text{slab})(X)_m} - (E_{\text{slab}} + mE_X)}{m},$$

where E_{ads} is average adsorption energy, $E_{(\text{slab})(X)_m}$ is the energy of the system after adsorption, E_{slab} is the energy of the substrate before adsorption, E_X is the energy of a single gas molecule, and m

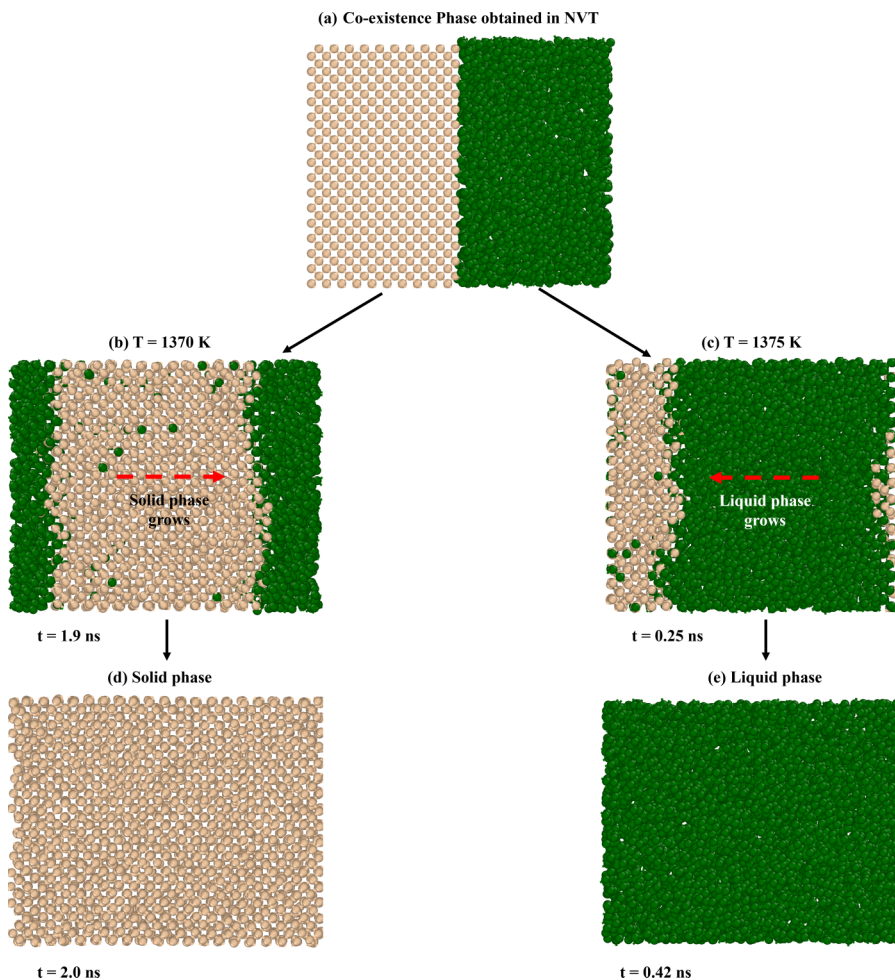


FIG. 2. Snapshots taken from the two-phase MD simulations. (a) Co-existence phase including liquid and solid of Si obtained in the NVT, (b) solid/liquid interface moving toward the liquid phase, (c) solid/liquid interface moving toward the crystal phase, (d) crystal phase completely overtaking liquid phase at 1370 K for 2.0 ns, (e) liquid phase filling the box at 1375 K for 0.42 ns.

07 September 2024 09:05:31

is the number of adsorbed gas molecules. The average adsorption energies for oxygen molecules on the pure Si (001) surface ($E_{\text{ads}(\text{Si})(\text{O}_2)}$), for water molecules on the pure Si (001) surface ($E_{\text{ads}(\text{Si})(\text{H}_2\text{O})}$), and for oxygen molecules on the Si (001) surface with the presence of hydrogen ($E_{\text{ads}(\text{SiH})(\text{O}_2)}$) were calculated. The structures used for the adsorption energy calculations were taken from the datasets corresponding to them in Sec. II A, and these structures come from either AIMD simulations.

From the results in Table IV, we can see that the results of the ML potential are very close to those of the DFT, while other

empirical potentials overestimate or underestimate the average adsorption energies. Meanwhile, $E_{\text{ads}(\text{SiH})(\text{O}_2)}$ is larger than $E_{\text{ads}(\text{Si})(\text{O}_2)}$, which indicates that hydrogen present on the silicon surface promotes the adsorption of oxygen molecules on the surface.

D. Simulation of thermal oxidation

Based on trained and validated potential, we carry out molecular dynamics simulations of the silicon thermal oxidation processes by Large-scale Atomic/Molecular Massively Parallel

TABLE II. Comparison of structural properties of Si based on a range of interatomic potentials, DFT, and experiments.

Property		DFT	ML	Reaxff _{Larsson}	Reaxff _{SiOH(2023)}	Experiment
c-Si	Melting point (K)	(1327–1401) ⁴⁰	(1370–1375)	(2365–2370)	(3440–3445)	1683 ⁴¹
	$a(\text{\AA})$	5.47	5.47	5.32	5.37	5.43 ⁴²
	$E_{\text{coh}}(\text{eV})$	−4.55	−4.55	−4.6	−4.75	−4.63 ⁴²
	Density (g/cm ³)	2.28	2.27	2.48	2.41	2.33 ⁴³
	$d_{\text{Si-Si}}$	2.37	2.37	2.31	2.325	2.368 ⁴⁴

TABLE III. Comparison of structural properties of a-SiO₂ based on a range of interatomic potentials, DFT, and experiments.

Property	DFT	ML	Reaxff _{Larsson}	Reaxff _{SiOH(2023)}	Experiment
Density (g/cm ³)	2.27	2.23	2.16	2.3	2.2 ⁴⁵
Si–O bond distance (Å)	1.62	1.62	1.63	1.61	1.608 ⁴⁶
Si–Si bond distance (Å)	3.1	3.1	3.15	3.1	
O–O bond distance (Å)	2.65	2.65	2.65	2.62	2.65 ⁴⁵
Si–O RDF first max (Å)	1.62	1.62	1.63	1.61	1.62 ⁴⁵
Si–Si RDF first max (Å)	3.12	3.12	3.14	3.11	3.12 ⁴⁵
O–O RDF first max (Å)	2.62	2.62	2.62	2.61	2.626 ⁴⁶
Si–O–Si (deg)	150.3	152.1	144.9	144.9	151.0 ⁴⁷
O–Si–O (deg)	108.9	108.9	108.9	108.9	109.5 ⁴⁶

Simulation (LAMMPS) Package.⁴⁹ Silicon substrate with $54.7 \times 54.7 \text{ \AA}^2$ area (the x–y plane) and 109.4 \AA depth (z-direction) was used for the simulations, with the periodic boundary condition in the plane direction. Fix the bottom two layers of atoms, insert O₂ molecules or H₂O molecules from the vacuum region at the top of the substrate, and simulate at 1073 and 1273 K. The time step for all simulated processes was set to 0.5 fs. The system was first equilibrated at zero external pressure and at the temperature required for the simulation (NPT ensemble) for 5 ps. When the oxidizer starts to insert, the x–y plane is divided into the center region where an NVE ensemble is used and the borders region (2 Å in length) using the NVT ensemble, this allows the kinetic energy of the ions to propagate through the phonons into the thermostatic region, thus keeping the system at a constant temperature. During the oxidation process, oxidizing agents are added to the box every 4000 steps with a time interval of about 2 ps. The number of oxygen atoms falling at a time is the same for both dry oxidation and wet oxidation, with three O₂ molecules falling at a time for dry oxidation, and two O₂ and two H₂O molecules each for wet oxidation. In order for the reaction to proceed smoothly, a kinetic energy of 5–10 eV was applied to the oxidizers, and the velocity of descent was calculated from their assigned kinetic energies. As the oxidation process proceeds, the rate of oxidation will gradually level off, and it is sufficient to choose to terminate the simulation when the oxidation rate is found to level off. Referring to the simulation work of Noaki *et al.*, we set the total time of each simulation to 2.5 ns and performed exactly the same simulation using the reactive force field as a comparison.

Figure 3 shows the numbers of oxygen atoms retained in the system over time for the ML potential and ReaxFF_{Larsson} at two temperatures T = 1073 and 1273 K. As can be seen in Fig. 3, the

oxidation rate is higher for wet oxidation than dry oxidation when using the ML force field for oxidation simulation, a phenomenon that is consistent with the results obtained in the experiments² and serves as an important benchmark for measuring the accuracy of the MD simulation of the silicon thermal oxidation process. The accumulation of oxygen atoms per unit of time in the system is decreasing throughout the oxidation process. At the initial stage of the oxidation process, before 0.3 ns, the dry and wet processes oxidize at close rates, after which the wet process oxidizes at a faster rate than the dry process. This is considered the acceleration of oxide growth observed in the wet process. The phenomenon does not occur in ReaxFF_{Larsson} as seen in Fig. 3(b). In addition, the oxidation rate has a temperature dependence, the higher the temperature, the faster the oxidation rate, which occurs because high temperatures make the diffusion of oxygen atoms easier. The temperature dependence of the oxidation rate is not reflected in the work of Noaki *et al.*¹⁵ This is due to the fact that the force field they used greatly overestimated the melting point of silicon.

In Fig. 4, the evolution of the Si(001) substrate structures subjected to dry/wet oxidation at T = 1073 K is shown. Changes in temperature do not affect the general stages of oxide growth discussed herein. Oxide growth can generally be divided into two stages, the primary oxidation stage, which is dominated by adsorption reactions, and the diffusion oxidation stage, which is dominated by diffusion reactions. The complete oxidation of several layers of atoms on the substrate surface is the dividing line between these two stages.

The first to occur is the primary oxidation stage since the reaction occurs at high temperatures, two to three layers of atoms on the substrate surface become disorganized and rebuild the surface prior to contact with the oxidant, and the rebuilt surface is more susceptible to reaction with the oxidant compared to an ordered surface. This can be demonstrated by comparing the oxygen atom increment at the early stages of oxidation in Figs. 3(a) and 3(b). Since the Reaxff_{Larsson} overestimates the melting point of silicon, the substrate surface is still in a crystalline state at 1073 K. This leads to an increase in the difficulty of the oxidation reaction, and thus, its oxygen atom increment at the early stages of oxidation is lower than the result of the ML potential at the same time. In the primary oxidation stage, the adsorption of the oxidant on the substrate surface is very strong, and the vast majority of the inserted oxidant is adsorbed on the surface, in general, oxygen molecules

TABLE IV. Comparison of average adsorption energy based on a range of interatomic potentials and DFT.

	E _{ads(Si)(O₂)} (eV)	E _{ads(Si)(H₂O)} (eV)	E _{ads(Si_H)(O₂)} (eV)
DFT	8.31	-1.22	9.160
ML	8.2	-1.50	9.53
Reaxff _{Larsson}	3.71	-4.69	9.74
Reaxff _{SiOH(2023)}	9.23	-13.43	17.62

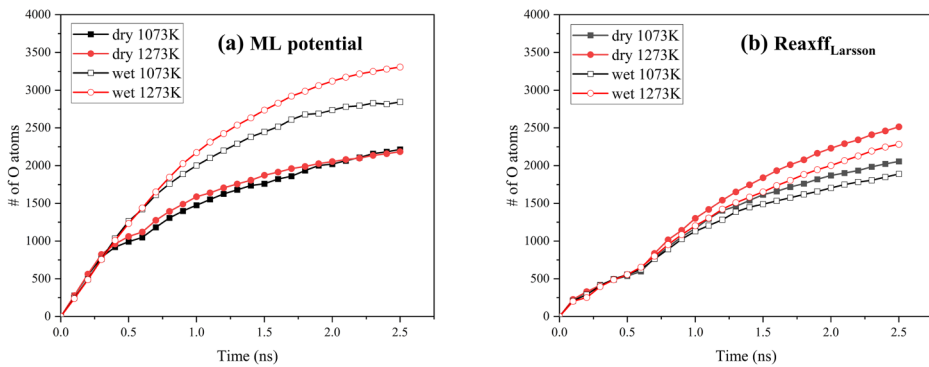


FIG. 3. Temporal variation of the number of oxygen atoms retained in the system during thermal oxidation of silicon. (a) Comparison of wet and dry processes in ML potential at $T = 1073$ K and 1273 K. (b) Comparison of wet and dry processes in ReaxFF_{Larsson} at $T = 1073$ and 1273 K.

07 September 2024 09:05:31

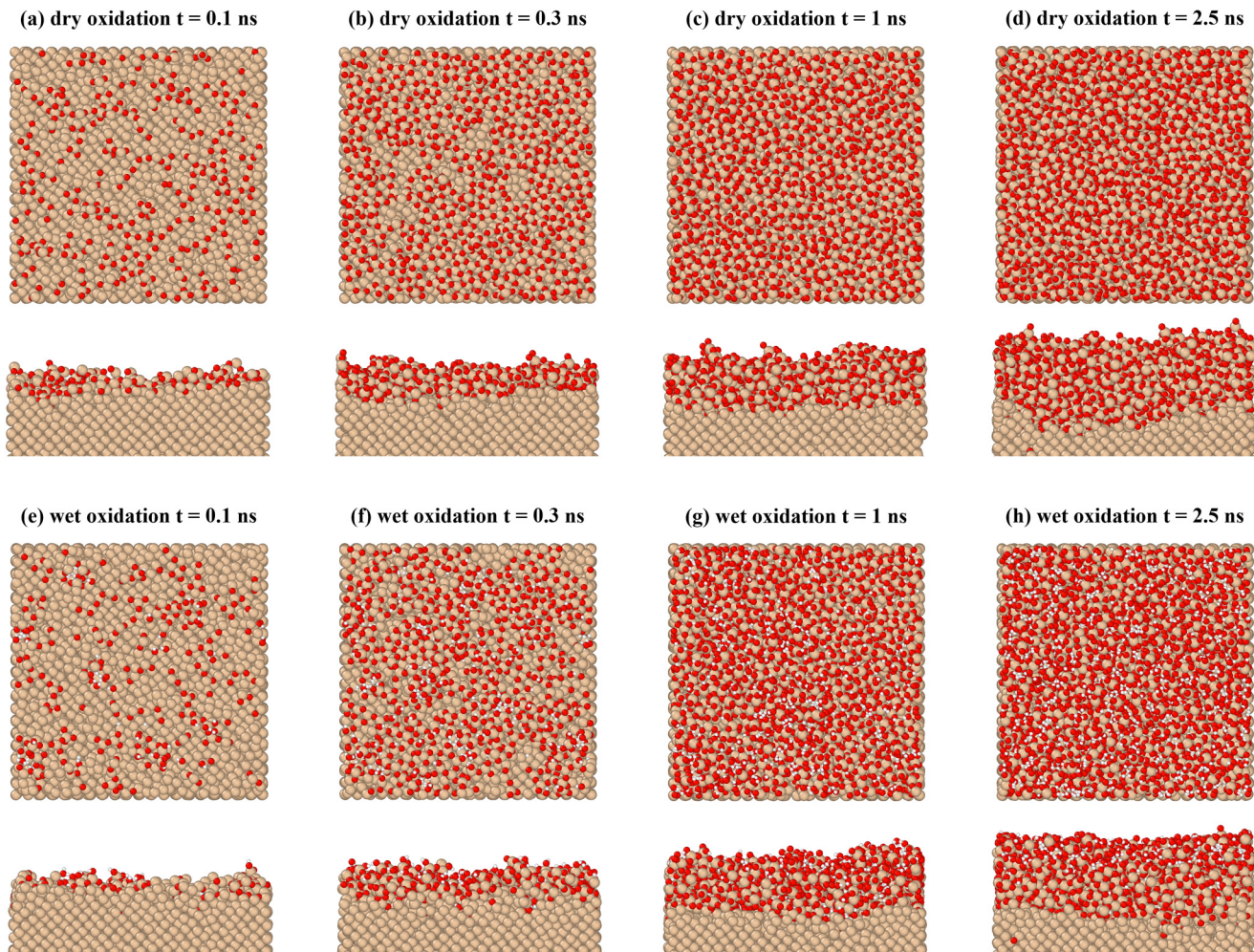


FIG. 4. Snapshots of the dry/wet oxidation structures of Si(001) slab at $T = 1073$ K at four different time points. (a)-(d) Schematic structure of dry oxidation at 0.1, 0.3, 1, and 2.5 ns. (e)-(h) Schematic structure of wet oxidation at 0.1, 0.3, 1, and 2.5 ns (OVITO).⁵⁰

dissociate into two oxygen atoms adsorbed on the silicon surface, and water molecules dissociate into hydrogen ion and hydroxyl adsorbed on the silicon surface. However, the adsorption at this stage is not homogeneous in either dry or wet oxidation, and the adsorbed atoms diffuse across the surface until they reach their most stable position. For example, the hydrogen in the hydroxyl may be captured by other silicon atoms in the subsequent relaxation process, and the surface hydrogen atoms may generate hydrogen with other surface hydrogen atoms to fly away in the migration process.

Afterward, with the increase of oxidant, the bonding between the surface silicon atoms and the lower silicon atoms is weakened, and a detachment phenomenon occurs between the oxidized layer and the layer below it, and oxidized islands and pure silicon basins are formed on the surface [Figs. 4(a) and 4(e)]. This surface morphology is crucial for the subsequent diffusive oxidation process. First, this detachment phenomenon lowers the barrier to diffusion of the oxidant to the subsurface sites. Second, this surface topography allows the oxidant to migrate to the subsurface sites and undergo oxidation reactions even before the surface adsorption sites are fully occupied. In Figs. 4(b) and 4(f), when the thickness of the oxide is about two to three atomic layers, there are still multiple regions on the surface that are not completely covered by the oxide. This allows the process to repeat between the oxide and the underlying silicon, reducing the difficulty of the subsequent diffusion oxidation process.

Beyond several layers of atoms on the surface completely oxidized, the oxidation process transitions from the primary stage to the diffusion oxidation stage. Since the previously generated oxide layer hinders the adsorption of the oxidant on the subsurface sites, both in dry and wet oxidation, the oxides in this stage rely mainly on the diffusion of the oxidant to the lower sites and their reaction with the silicon, which results in a lower rate of oxide generation than in the primary stage. This can also be visualized by comparing the structural diagrams of $t = 1$ and 2.5 ns.

Finally, based on the simulation results of ML potential, the analysis obtained is that the presence of hydrogen in the system is the most important reason for the faster oxidation rate of wet oxidation than dry oxidation. From the calculations in Sec. III C, the average adsorption energy of oxygen molecules on the silicon surface with the presence of hydrogen is higher than that on the silicon surface without hydrogen, which indicates that the substrate

surface absorbs oxygen molecules more readily under wet oxidation conditions than dry oxidation. Furthermore, the hydrogen present in the oxide and interfacial regions reduces the migration barrier for oxygen atoms,⁹ and the lowering of the barrier indicates that oxygen atoms migrate more readily, and more readily migrated oxygen atoms mean that oxidation reactions in the diffusion oxidation stage are more likely to occur. The coupling of these two factors leads to the phenomenon of oxidation acceleration in wet oxidation.

E. Annealing and defect analysis

In the production of semiconductor devices, the manufacturing process of silicon oxide usually includes an annealing process. This is to improve the quality of the silicon oxide film and to facilitate subsequent processes such as lithography and etching.⁵¹ Here, we annealed the oxidized structures. The oxidized structures were cooled down to 300 K at a rate of 5 K/ps under the NPT ensemble and continued to relax at 300 K for 10 ps to reach equilibrium.⁵² After that, the typical defect information in the oxidized layer before and after annealing were compared.

The first step in the defect analysis is to determine the coordination of each atom based on the truncation radius. Since the structure analyzed is a-SiO_2 , the interatomic bond length is not a fixed value, so the cutoff radius should be set slightly larger than the average interatomic bond length, and the cutoff radius used in this paper is 1.1 times the average interatomic bond length. After determining the coordination of each atom, the local configuration where the atom is located is analyzed, and if the configuration matches the configuration of ODC or NBOHC, the configuration is a typical defect. In the case of ODC, for example, after the coordination of each atom in the system has been determined, if the presence of Si–Si bonds is detected and each of the two silicon atoms is bonded to three oxygen atoms, then this is an ODC defect.

The change in the number of defects in the oxide layer before and after annealing is shown in Fig. 5. From Fig. 5(a), it can be seen that before annealing, NBOHCs exist in the system both as dry oxide obtained by dry oxidation and wet oxide obtained by wet oxidation, and the number of NBOHCs in the wet oxide is more than that in the dry oxide. By analyzing the oxidation process and based on the experimentally obtained reaction equations for the generation of NBOHCs,⁵³ it is possible to explain the difference in

07 September 2024 09:05:31

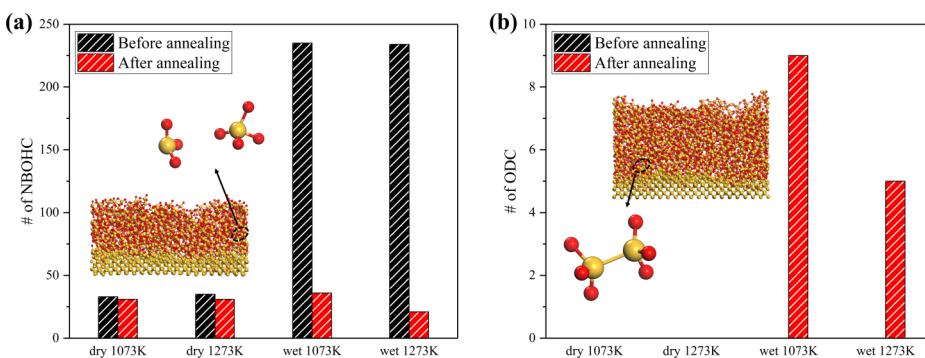


FIG. 5. Comparison of the number of typical defects in the oxide layer before and after annealing. (a) Nonbridging oxygen hole center (NBOHC). (b) Oxygen deficiency centers (ODCs).

the amount of NBOHCs in the oxides obtained by dry and wet oxidation before annealing. There are two proposed reactions for the production of NBOHCs, in the oxygen excess environment as $\equiv\text{Si}-\text{O}-\text{O}-\text{Si}\equiv \rightarrow \equiv\text{Si}-\text{O}\cdot + \cdot\text{O}-\text{Si}\equiv$, $\equiv\text{Si} + \text{O} \rightarrow \equiv\text{Si}-\text{O}\cdot$ and in high-OH type as $\equiv\text{Si}-\text{OH} \rightarrow \equiv\text{Si}-\text{O}\cdot + \text{H}^0$ ($\equiv\text{Si}$, $-$ represents a Si-O bond, and \cdot represents an unpaired electron). During wet oxidation, water molecules dissociate into hydrogen ions and hydroxyl groups and react with silicon, resulting in the generation of a large amount of Si-OH in the system, more precursors mean that NBOHCs are more likely to be generated, which ultimately leads to the difference in the number of NBOHCs in the wet and dry oxides before annealing.

The number of NBOHC defects in both the dry and wet oxides decreased after annealing was completed, which was due to NBOHC healing during the annealing process. Local structural changes containing defects during the NBOHC healing process are shown in Fig. 6(a) to Fig. 6(c). As the annealing process proceeds, the atoms in the structure keep moving and the distance between the non-bridging oxygen and the neighboring silicon gradually decreases, after which a stable Si-O bond is formed. Oxygen previously connected to neighboring silicon bonds with its surrounding

silicon upon disconnection and migrates to the stable state during the subsequent relaxation process. The number of NBOHCs in the wet oxides decreases more than in the dry oxides, which indicates that larger-scale structural healing occurs in the wet oxides. In the annealing process, due to the role of stress, the hydrogen bond in the wet oxide is broken, resulting in a lot of unsaturated silicon and free hydrogen atoms, at which time most of the free hydrogen atoms become hydrogen gas and escape, and a small number of hydrogen atoms diffuse into the interface between the oxide layer and the silicon and the interface at the silicon to form a Si-H structure. After that, the structure is reconfigured during the annealing process, where the unsaturated silicon reacts with the NBOHCs to form an intact structure, and the number of NBOHCs in the system decreases.

As for ODC, it behaves differently from NBOHC. As shown in Fig. 5(b), the presence of ODCs was not found in both dry and wet oxides before annealing, and, after annealing, ODCs were also found only in wet oxides. We traced the generation of ODCs in wet oxides as shown in Fig. 6(d) through Fig. 6(f). For ease of illustration, the O atoms undergoing migration are numbered sequentially and labeled in the figure. The ODCs evolve from the

07 September 2024 09:05:31

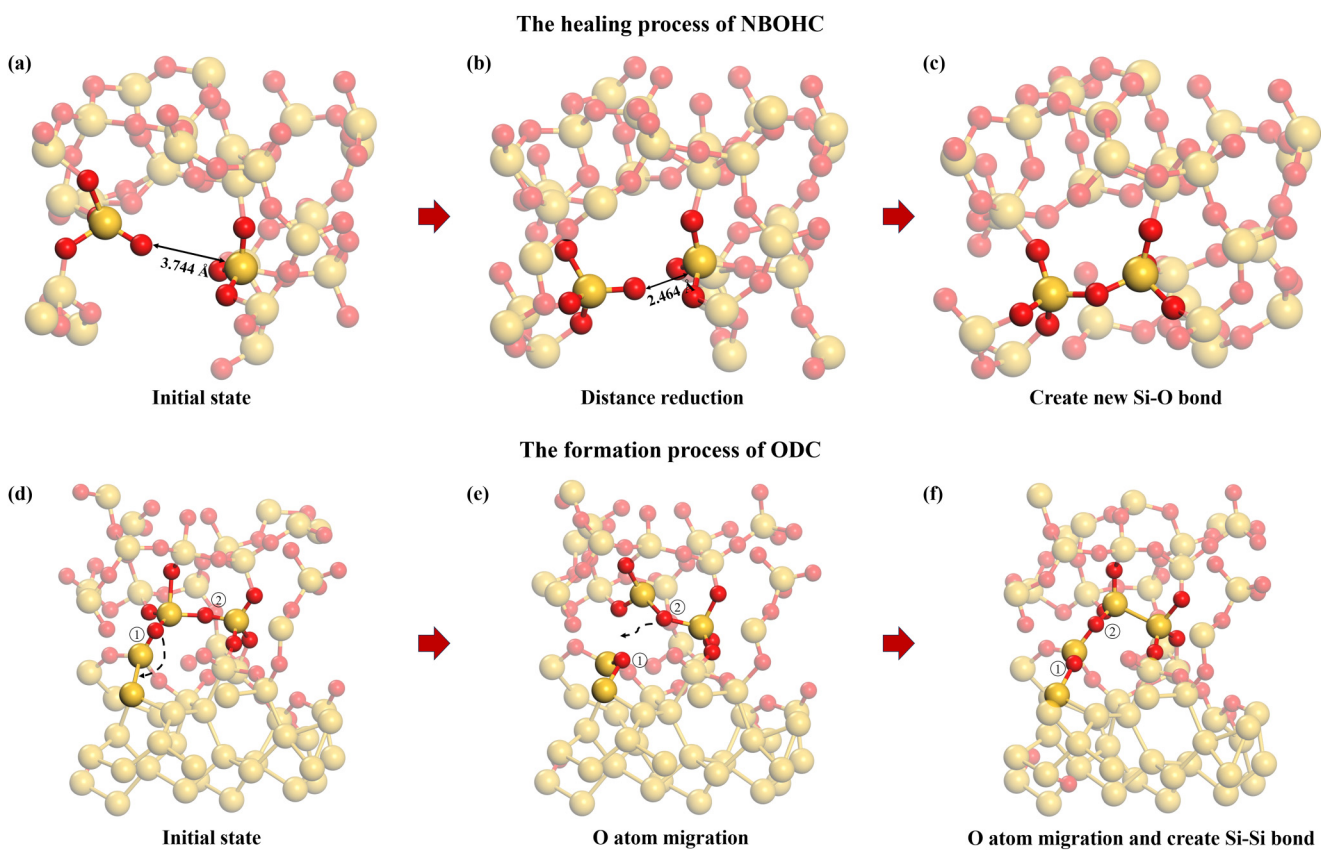


FIG. 6. The evolution process of NBOHC and ODC. (a)–(c) The healing process of NBOHC. (d)–(f) The formation process of ODC; the dashed arrows indicate the migration of the oxygen atoms that will occur.

$\equiv\text{Si}-\text{O}-\text{Si}\equiv$ structure, and the first step in the evolution is the migration of oxygen atom ① into the middle of the two near-neighboring silicon atoms, bonding with them and creating an oxygen vacancy in its place. Meanwhile, oxygen atom ② moves from its position away from the vacancy to a position close to the vacancy in preparation for the upcoming migration. Next, oxygen atom ② migrates into the vacancy left by oxygen atom ①, and the two silicon atoms originally connected to oxygen atom ② form Si-Si bond, and the complete structure evolves into an ODC. In this process, when oxygen atom ① migrates to the middle of two near-neighboring silicon atoms, oxygen atom ① will form a Si-O-Si triangular configuration with the two silicon atoms connected to it, as in Fig. 6(e); before the migration of oxygen atom ②, the distance between the two silicon atoms linked to oxygen atom ② will be gradually close to each other due to the movement of oxygen atom ②, the Si-O-Si triangular configuration will also be formed which is similar to the discovery of Khalilov *et al.*⁵⁴ and Yang *et al.*⁵⁵ Furthermore, the higher the oxidation temperature, the lower the number of defects in the annealed oxide. This is because higher temperatures require longer annealing to cooldown when reduced to the same temperature, and the longer the annealing time, the better the annealing of the structure, and the fewer defects that remain in the structure.

IV. CONCLUSIONS

In this paper, we constructed a large DFT dataset containing conformations related to static properties, defects related properties, and silicon oxidation process. Based on this dataset, we constructed an accurate and efficient ML potential with DFT accuracy that can be used to describe the thermal oxidation process of silicon.

After obtaining the ML potential, we calculate the melting point and structural properties of silicon, the structural properties of a-SiO₂, and the adsorption properties on the silicon surface, and the results agree well with the DFT and experiment reference data and are better than the ReaxFF. Then, we performed thermal oxidation simulations based on the ML potential and discussed the oxide growth process in detail. We elucidate that the oxidation acceleration mechanism of wet oxidation can be attributed to the fact that hydrogen in the wet oxide system both enhances the adsorption of oxygen on the silicon surface and promotes the migration of oxygen atoms. Finally, we annealed the oxidized structure, counting the defect information in the structure before and after annealing and analyzing the defect evolution behavior during the annealing process. We found the presence of NBOHCs in the structure before and after annealing in both dry and wet oxides, and the NBOHCs undergo healing during the annealing process. ODCs were found only in the wet oxide after annealing, which indicates that the oxide layer generated by dry oxidation has a stronger densification. Observation of the structure suggests that the ODCs formation in the wet oxide is due to the migration of O atoms in the $\equiv\text{Si}-\text{O}-\text{Si}\equiv$ structure.

ACKNOWLEDGMENTS

This work is supported by the National Science Foundation of China under Grant Nos. 12172112, 52293372, 11932005, and 11974091 and the National Natural Science Foundation of China

(Joint Fund for Corporate Innovation and Development—Key Program, Grant No. U22B2082).

AUTHOR DECLARATIONS

Conflict of Interest

The authors have no conflicts to disclose.

Author Contributions

Huyang Li: Conceptualization (equal); Data curation (equal); Formal analysis (equal); Investigation (equal); Methodology (equal); Writing – original draft (lead); Writing – review & editing (lead). **Yuhang Jing:** Conceptualization (equal); Formal analysis (equal); Writing – review & editing (equal). **Zhongli Liu:** Conceptualization (equal); Formal analysis (equal); Investigation (equal); Validation (equal); Writing – review & editing (equal). **Lingzhi Cong:** Formal analysis (equal); Investigation (equal); Validation (equal). **Junqing Zhao:** Investigation (supporting); Resources (supporting). **Yi Sun:** Investigation (supporting); Resources (supporting). **Weiqi Li:** Software (supporting); Validation (supporting). **Jihong Yan:** Resources (supporting). **Jianqun Yang:** Methodology (supporting); Resources (equal); Visualization (equal); Writing – review & editing (supporting). **Xingji Li:** Conceptualization (equal); Investigation (equal); Methodology (equal); Resources (lead); Supervision (lead); Visualization (equal); Writing – review & editing (equal).

DATA AVAILABILITY

The data that support the findings of this study are available from the corresponding author upon reasonable request.

REFERENCES

- ¹D. Muller, T. Sorsch, S. Moccio *et al.*, “The electronic structure at the atomic scale of ultrathin gate oxides,” *Nature* **399**, 758–761 (1999).
- ²B. E. Deal and A. S. Grove, “General relationship for the thermal oxidation of silicon,” *J. Appl. Phys.* **36**(12), 3770–3778 (1965).
- ³D. Hisamoto *et al.*, “FinFET-a self-aligned double-gate MOSFET scalable to 20 nm,” *IEEE Trans. Electron Devices* **47**(12), 2320–2325 (2000).
- ⁴H. H. Mueller and M. Schulz, “Individual interface traps at the Si–SiO₂ interface,” *J. Mater. Sci.: Mater. Electron.* **6**, 65–74 (1995).
- ⁵T. Umeda *et al.*, “Electron spin resonance observation of the Si (111)- (7 × 7) surface and its oxidation process,” *Phys. Rev. Lett.* **86**(6), 1054–1057 (2001).
- ⁶B. H. Kim *et al.*, “Effects of suboxide layers on the electronic properties of Si (100)/SiO₂ interfaces: Atomistic multi-scale approach,” *J. Appl. Phys.* **113**, 073705 (2013).
- ⁷D. Cadavid and A. Cabot, “Oxidation at the atomic scale,” *Science* **356**(6335), 245 (2017).
- ⁸C. Yang, C. Yang, P. Huang *et al.*, “First-principles study of the adsorption and diffusion of O₂ on a Si(001) surface,” *Surf. Rev. Lett.* **18**(6), 315–321 (2011).
- ⁹R. B. Capaz, L. V. C. Assali, L. C. Kimerling *et al.*, “Mechanism for hydrogen-enhanced oxygen diffusion in silicon,” *Phys. Rev. B* **59**(7), 4898–4900 (1999).
- ¹⁰H. Watanabe, K. Kato, T. Uda *et al.*, “Kinetics of initial layer-by-layer oxidation of Si(001) surfaces,” *Phys. Rev. Lett.* **80**(2), 345–348 (1998).
- ¹¹S. Takamoto *et al.*, “Charge-transfer interatomic potential for investigation of the thermal-oxidation growth process of silicon,” *J. Appl. Phys.* **120**(16), 165109 (2016).

- ¹²A. C. T. van Duin, A. Strachan, S. Stewman *et al.*, “ReaxFF SiO reactive force field for silicon and silicon oxide systems,” *J. Phys. Chem. A* **107**(19), 3803–3811 (2003).
- ¹³H. R. Larsson, A. C. T. van Duin, and B. Hartke, “Global optimization of parameters in the reactive force field ReaxFF for SiOH,” *J. Comput. Chem.* **34**, 2178–2189 (2013).
- ¹⁴N. Nayir, A. C. T. van Duin, and S. Erkoc, “Development of the ReaxFF reactive force field for inherent point defects in the Si/silica system,” *J. Phys. Chem. A* **123**, 4303–4313 (2019).
- ¹⁵J. Noaki, S. Numazawa, J. Jeon *et al.*, “Development of the reactive force field and silicon dry/wet oxidation process modeling,” *npj Comput. Mater.* **9**, 161 (2023).
- ¹⁶L. Zhang, J. Han, H. Wang, R. Car, and W. E, “Deep potential molecular dynamics: A scalable model with the accuracy of quantum mechanics,” *Phys. Rev. Lett.* **120**(14), 143001 (2018).
- ¹⁷K. T. Butler, D. W. Davies, H. Cartwright, O. Isayev, and A. Walsh, “Machine learning for molecular and materials science,” *Nature* **559**, 547–555 (2018).
- ¹⁸A. P. Bartók, M. C. Payne, R. Kondor *et al.*, “Gaussian approximation potentials: The accuracy of quantum mechanics, without the electrons,” *Phys. Rev. Lett.* **104**(13), 136403 (2010).
- ¹⁹O. T. Unke *et al.*, “Machine learning force fields,” *Chem. Rev.* **121**(16), 10142–10186 (2021).
- ²⁰J. Behler and M. Parrinello, “Generalized neural-network representation of high-dimensional potential-energy surfaces,” *Phys. Rev. Lett.* **98**, 146401 (2007).
- ²¹J. Behler *et al.*, “Pressure-induced phase transitions in silicon studied by neural network-based metadynamics simulations,” *Phys. Status Solidi B* **245**(12), 2618–2629 (2008).
- ²²A. P. Bartók, J. Kermode, N. Bernstein, and G. Csányi, “Machine learning a general purpose interatomic potential for silicon,” *Phys. Rev. X* **8**(4), 041048 (2018).
- ²³N. Artrith and J. Behler, “High-dimensional neural network potentials for metal surfaces: A prototype study for copper,” *Phys. Rev. B* **85**(4), 045439 (2012).
- ²⁴Y. Xia and P. Sautet, “Plasma oxidation of copper: Molecular dynamics study with neural network potentials,” *ACS Nano* **16**(12), 20680–20692 (2022).
- ²⁵Z. Y. Wang, Y. H. Jing *et al.*, “A machine-learning interatomic potential to understand the anisotropic fracture behavior of BaZrO₃ material,” *Solid State Ionics* **401**, 116358 (2023).
- ²⁶Z. Y. Wang, Y. H. Jing *et al.*, “Hydration induced mechanical degradation in the Y-doped BaZrO₃ solid oxide,” *Comput. Mater. Sci.* **235**, 112824 (2024).
- ²⁷J. L. Zhao, J. Byggmästar *et al.*, “Complex Ga₂O₃ polymorphs explored by accurate and general-purpose machine-learning interatomic potentials,” *npj Comput. Mater.* **9**, 159 (2023).
- ²⁸H. W. Niu *et al.*, “On the anomalous diffusion of proton in Y-doped BaZrO₃ perovskite oxide,” *Solid State Ionics* **376**, 115859 (2022).
- ²⁹H. W. Niu, Y. B. Yang, S. Jensen *et al.*, “Stable solid molecular hydrogen above 900 K from a machine-learned potential trained with diffusion quantum Monte Carlo,” *Phys. Rev. Lett.* **130**(7), 076102 (2023).
- ³⁰H. W. Niu *et al.*, “A machine-learning interatomic potential to understand primary radiation damage of silicon,” *Comput. Mater. Sci.* **218**, 111970 (2023).
- ³¹A. Hamedani, J. Byggmästar *et al.*, “Insights into the primary radiation damage of silicon by a machine learning interatomic potential,” *Mater. Res. Lett.* **8**(10), 364–372 (2020).
- ³²G. Kresse and J. Furthmüller, “Efficiency of ab-initio total energy calculations for metals and semiconductors using a plane-wave basis set,” *Comput. Mater. Sci.* **6**(1), 15–50 (1996).
- ³³G. Kresse and D. Joubert, “From ultrasoft pseudopotentials to the projector augmented-wave method,” *Phys. Rev. B* **59**(3), 1758 (1999).
- ³⁴G. Kresse and J. Furthmüller, “Efficient iterative schemes for *ab initio* total-energy calculations using a plane-wave basis set,” *Phys. Rev. B* **54**(16), 11169 (1996).
- ³⁵J. P. Perdew, K. Burke, and M. Ernzerhof, “Generalized gradient approximation made simple,” *Phys. Rev. Lett.* **77**(18), 3865 (1996).
- ³⁶H. Wang *et al.*, “DeePMD-kit: A deep learning package for many-body potential energy representation and molecular dynamics,” *Comput. Phys. Commun.* **228**, 178–184 (2018).
- ³⁷J. Z. Zeng *et al.*, “DeePMD-kit v2: A software package for deep potential models,” *J. Chem. Phys.* **159**, 054801 (2023).
- ³⁸J. Behler, “Constructing high-dimensional neural network potentials: A tutorial review,” *Int. J. Quantum Chem.* **115**(16), 1032–1050 (2015).
- ³⁹X. W. Wang *et al.*, “A comprehensive investigation on the accuracy and efficiency of methods for melting temperature calculation using molecular dynamics simulations,” *J. Mol. Liq.* **395**, 123924 (2024).
- ⁴⁰Q.-J. Hong and A. van de Walle, “Solid-liquid coexistence in small systems: A statistical method to calculate melting temperatures,” *J. Chem. Phys.* **139**(9), 094114 (2013).
- ⁴¹A. Kubo *et al.*, “Melting curve of silicon to 15 GPa determined by two-dimensional angle-dispersive diffraction using a Kawai-type apparatus with X-ray transparent sintered diamond anvils,” *J. Phys. Chem. Solids* **69**, 2255–2260 (2008).
- ⁴²M. T. Yin and M. L. Cohen, “Theory of static structural properties, crystal stability, and phase transformations: Application to Si and Ge,” *Phys. Rev. B* **26**(10), 5668 (1982).
- ⁴³I. Henins, “Precision density measurement of silicon,” *J. Res. Natl. Bur. Stand., Sect. A* **68A**, 529 (1964).
- ⁴⁴K. Persson, “Materials data on Si (SG:227) by materials project,” *Mater. Proj.* (2014).
- ⁴⁵R. L. Mozzi and B. E. Warren, “The structure of vitreous silica,” *J. Appl. Crystallogr.* **2**, 164–172 (1969).
- ⁴⁶D. I. Grimley *et al.*, “Neutron scattering from vitreous silica IV. Time-of-flight diffraction,” *J. Non-Cryst. Solids* **119**, 49–64 (1990).
- ⁴⁷F. Mauri *et al.*, “Si–O–Si bond-angle distribution in vitreous silica from first-principles ²⁹Si NMR analysis,” *Phys. Rev. B* **62**, R4786–R4789 (2000).
- ⁴⁸M. Galyńska and P. Persson, “Chapter eight—Material dependence of water interactions with metal oxide nanoparticles: TiO₂, SiO₂, GeO₂, and SnO₂,” *Adv. Quantum Chem.* **69**, 303–332 (2014).
- ⁴⁹S. Plimpton, “Fast parallel algorithms for short-range molecular dynamics,” *J. Comput. Phys.* **117**(1), 1–19 (1995).
- ⁵⁰A. Stukowski, “Visualization and analysis of atomistic simulation data with OVITO—The open visualization tool,” *Modell. Simul. Mater. Sci. Eng.* **18**, 015012 (2010).
- ⁵¹M. Quirk and J. Serda, *IC Fabrication Process Overview. Semiconductor Manufacturing Technology* (Prentice Hall, 2001), Chap. 9.
- ⁵²P. Pal, V. Swarnalatha, A. V. N. Rao *et al.*, “High speed silicon wet anisotropic etching for applications in bulk micromachining: A review,” *Micro Nano Syst. Lett.* **9**, 4 (2021).
- ⁵³H. Nishikawa, “Structures and properties of amorphous silicon dioxide—issues on the reliability and novel applications,” in *Silicon-Based Material and Devices* (Academic Press, 2001), Chap. 3, Vol. 2, pp. 93–122.
- ⁵⁴U. Khalilov *et al.*, “On the c-Si/a-SiO₂ interface in hyperthermal Si oxidation at room temperature,” *J. Phys. Chem. C* **116**, 21856–21863 (2012).
- ⁵⁵T.-C. Yang and K. C. Saraswat, “Effect of physical stress on the degradation of thin SiO₂ films under electrical stress,” *IEEE Trans. Electron Devices* **47**(4), 746–755 (2000).